Partial-field decomposition analysis of full-scale supersonic jet noise using optimized-location virtual references

Alan T. Wall, Kent L. Gee, Kevin M. Leete, Tracianne B. Neilsen, Trevor A. Stout, and Michael M. James

Citation: The Journal of the Acoustical Society of America **144**, 1356 (2018); doi: 10.1121/1.5053580
View online: https://doi.org/10.1121/1.5053580
View Table of Contents: https://asa.scitation.org/toc/jas/144/3
Published by the Acoustical Society of America

Partial-field decomposition analysis of full-scale supersonic jet noise using optimized-location virtual references

Alan T. Wall[a)]
Air Force Research Laboratory, Battlespace Acoustics Branch, Wright-Patterson Air Force Base, Dayton, Ohio 45433, USA

Kent L. Gee, Kevin M. Leete, Tracianne B. Neilsen, and Trevor A. Stout
Department of Physics and Astronomy, N283 ESC, Brigham Young University, Provo, Utah 84602, USA

Michael M. James
Blue Ridge Research and Consulting, LLC, Asheville, North Carolina 28801, USA

(Received 1 December 2017; revised 17 August 2018; accepted 22 August 2018; published online 12 September 2018)

Supersonic jet noise reduction efforts benefit from targeted source feature extraction and high-resolution acoustic imaging. Another useful tool for feature extraction is partial field decomposition of sources into independent contributors. Since such decomposition processes are nonunique, care must be taken in the physical interpretation of decomposed partially coherent aeroacoustic fields. The optimized-location virtual reference method (OLVR) is a partial field decomposition designed to extract physically meaningful source and field information through the strategic placement of virtual references within a reconstructed field. The OLVR method is applied here to obtain spatially distinct and ordered partial sources at multiple frequencies of a full-scale, high-performance supersonic jet engine operating at 100% engine power. Partial sources are shown to mimic behaviors of the total source distributions including monotonic growth and decay. Because of finite spatial coherence, multiple partial sources are used to reproduce far-field radiation away from the main lobe, and the number of required sources increases with increasing frequency. An analytical multi-wavepacket model is fitted to the partial sources to demonstrate how OLVR partial fields can be leveraged to produce reduced-order models. https://doi.org/10.1121/1.5053580

[SKT] Pages: 1356–1367

I. INTRODUCTION

There is a need to understand noise sources within high-speed tactical aircraft jet engines; this understanding can inform identification of noise reduction strategies to counteract potentially greater sound levels from higher-performance engines. Throughout the jet noise community, efforts are underway to correlate turbulent jet source mechanisms to equivalent acoustic source models, simulations, and measurements. These efforts can be enhanced through high-resolution imaging of jet noise sources and subsequent decomposition into subsource components that comprise the total radiated field. This paper presents an optimization method for isolating independent source components of jet noise based on near-field acoustical holography (NAH) source reconstructions. It also demonstrates how these source reconstructions can be leveraged to yield reduced-order, analytical wavepacket models of each partial source.

Partial field decomposition (PFD) of a sound field results in a set of mutually incoherent partial fields (PF), which can be summed energetically to represent the total field. PFD has been used to determine characteristic phase velocities of jet noise source components;[1] investigate spatiotemporal characteristics of the primary sources;[2] model field coherence properties;[3,4] and separate shock-associated noise, screech, and other components from the jet mixing noise.[5] In essence, PFD is often employed to simplify the representation of partially coherent, collocated or overlapping jet noise sources. However, neither the PFD process nor the resulting PFs are unique. The desired information about the source should dictate the decomposition method used. For example, decomposition methods that result in low-order models (the inclusion of the dominant energy in one or very few terms) are commonly used to obtain PFs for the turbulent flow,[6,7] for the radiated acoustic field,[8,9] to investigate correlations between flow and radiation,[1,10–12] and to serve as wavepacket models for sound field predictions.[4,10,13–15] These methods, motivated by efficiency, typically employ a singular value decomposition (SVD) of the cross-spectral matrix of flow or acoustic field information. An advantage of these methods is that equivalent source characteristics related to the most dominant field energies can be extracted. One disadvantage is that the PFs, when viewed independently, may have limited physical significance because information from multiple independent sources are combined into each PF.[1,16] Unfortunately, researchers often overstate the physical significance of the PFs, such as the assertion that a spatially extensive PF is the result of an extended, highly spatially coherent source mechanism. Photiadis[17] countered this argument by showing that an SVD-based decomposition of data arranged into simple shapes approach a mode-like decomposition, such as waves on a string for a long source

[a)]Electronic mail: alan.wall.4@us.af.mil

(see also Ref. 18). Vold *et al.*[3] showed that the azimuthal decomposition of a jet model with random (incoherent) azimuthal turbulence events decomposes into cylindrical modes with the SVD-based PFD.

The desire to isolate independent source mechanisms when multiple sources (or a source distribution of finite coherence) are present motivates an alternative approach to PFD. Most successful in generating physically relevant PFs are PFD techniques that use reference data collected as close as possible to each subsource[19] to obtain a basis set of terms that includes information almost exclusively from one source and excludes information from all others. In this paper, a PFD method called optimized-location virtual reference (OLVR)[18,20] is discussed. This method is used to isolate what might be considered "independent" equivalent noise sources in a jet, through the strategic spatial placement of *virtual* references (VR) along the source region, followed by a spatially iterative PFD. Although PFs resulting from OLVR are non-unique, they can be deliberately designed to target and extract physical source and field properties based on spatial coherence.

The OLVR method is based largely on a technique by Kim *et al.*,[16] who developed a post-NAH PFD procedure that made it possible to identify optimal VR locations for two independent loudspeakers, and then to decompose the field from VRs placed at those locations. Other PFD methods that utilize VRs exist,[21–23] but the Kim *et al.* approach was developed specifically to find the optimal VR locations, which were defined as the locations at which the multiple signal classification (MUSIC) power[19] was maximized in the region near the sources. The MUSIC power quantified the likelihood of finding actual sources within a set of candidate source locations. In the Kim *et al.* approach, since the pressures at these candidate locations could not be measured directly, the necessary sound pressures for the MUSIC algorithm were obtained from a projection of the measured sound field toward the sources with NAH. The result was a set of two physically meaningful PFs, where each PF was dominated by information from one and only one independent source.

The definition of what constitutes an independent source in jet noise is ambiguous, since a turbulent flow field represents a "smearing" of extended sources with spatially decaying coherence. Jet noise cannot be described as a single coherent source, nor as a distribution of completely independent sources, but lies somewhere in between. Thus, the enhancement to the Kim *et al.* method that makes OLVR unique lies in the advanced VR selection process. In order to obtain physically meaningful spatial distributions of PFs along the length of a jet axis, and account for partially coherent sources, the VRs selected here are optimized to have high MUSIC powers and low mutual coherence and to be spatially ordered. It should be noted that a different VR selection process with a different goal (i.e., the isolation of two partially independent radiation features) was implemented in a previous study,[24] emphasizing the fact that PFD is a nonunique process and the desired information dictates the method.

Holographic projection of the jet noise field for a full-scale high-performance jet was reported previously.[25] In this paper, OLVR is implemented on these latter reconstructions, selecting VRs from NAH reconstructions along a cylinder close to the jet. The resulting PFs are presented for multiple frequencies, and frequency-dependent source behaviors are discussed. Finally, wavepacket models are produced through fitting of analytical functions to the resulting partial sources. The result is a straightforward multiwavepacket representation of the full-scale jet that mimics physically relevant source parameters.

II. EXPERIMENT

A brief summary of the full experiment[26] is provided in this section. Hologram sound pressures in the near field of a full-scale jet installed on a high-performance aircraft were recorded with a 5×18 array of microphones, which had 15 cm (6 in.) spacing. The scans covered an approximately $2\,\text{m} \times 24\,\text{m}$ vertical planar region (i.e., the "hologram"), 5.6 m from the approximate shear layer region, shown in Fig. 1. Figure 1 specifies the coordinate system used in this experiment, with the origin on the ground directly below the jet nozzle, and the $+y$ axis pointing up (out of the page). Reference microphones (dots in Fig. 1) were also used to generate self-coherent holograms from the scans via a preliminary SVD-based PFD.[27] During each scan, a single high-performance engine was operated at 100% engine thrust request (ETR) (full or military power), while the second engine was held at idle power.

III. OLVR METHODOLOGY

The OLVR method encompasses various sub-algorithms to achieve the primary objective: physically meaningful PFs. To this end, the "optimization" process in optimized-location virtual reference PFD can be modified according to the desired source/field information. For example, the target of a previous investigation was to separate the incoherent contributions of two jet radiation lobes, so the two VRs were simply located in the far field near the center of each lobe.[24] In the current work, contributions to the field from isolated source components (based on their spatial coherence in the near field) are desired.

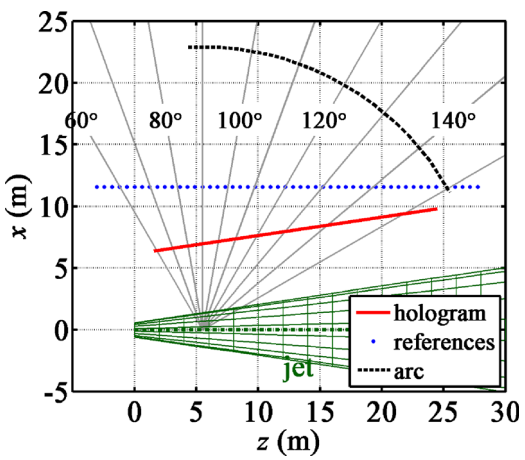

FIG. 1. (Color online) Top-down schematic of the measurement locations relative to the jet.

The OLVR procedure used here relies on the subprocesses of back propagation toward the source through the use of NAH, a PFD method based on a singular value decomposition (SVD-based PFD),[27] the MUSIC algorithm,[19,23] and the Gauss elimination technique (Cholesky decomposition) that is integral to a second PFD algorithm called partial coherence decomposition (PCD).[28] Note that the processes, listed in Table I, are performed independently for each frequency. Each sub-algorithm is now described in detail.

A. NAH sound field reconstruction

For sound fields generated by multiple, independent sources, a multi-reference PFD procedure must be used to obtain mutually incoherent PFs before NAH is implemented. Although detailed descriptions of these methods are not provided here, the reader is directed to Refs. 21 and 27 for the theoretical development of SVD-based PFD. In summary, SVD-based PFD generates mutually incoherent PFs from a measured hologram. To obtain these, an SVD of the cross spectrum of measured complex pressures at the physical references is performed, resulting in a linearly independent basis. These singular vectors represent new references; as the measured field is projected onto these new references, a linearly independent set of PFs is generated. These PFs are ordered such that their relative strengths decrease monotonically. These PFs do not necessarily correspond to independent sources, even though the PFs are themselves linearly independent.

The next step is to perform an NAH reconstruction of the sound field in the proximity of the source. Multisource statistically optimized near-field acoustical holography (M-SONAH)[29] is used as it incorporates multiple, spatially distinct sources into the wave-function expansion of the field. Since the jet noise was measured over a concrete run-up pad, a rigid reflection created an interference pattern in the hologram. Thus, in M-SONAH, the sound field is modeled as two sets of cylindrical wave functions, one that is centered on the centerline of the jet, and a second set centered on the reflected image of the jet below the reflecting plane. Accuracy of the reconstructions were demonstrated in Ref. 25.

The mathematical formulation for acoustic field reconstruction begins with placing the PFs into the rows of a matrix $\mathbf{P}$. For clarity in the following discussion, matrix dimensions are specified by superscripts, e.g., $\mathbf{P}^{L\times I}$, where L is the number of partial fields and I is the number of hologram grid points. The acoustic field at a set of reconstruction points, R, can be represented by

$$\mathbf{Y}' = \mathbf{H}_{\mathbf{yp}}\mathbf{P}, \tag{1}$$

where $\mathbf{Y}'^{R\times L}$ is the matrix containing the entire set of L partial fields reconstructed on the surface at all R reconstruction locations, and $\mathbf{H}_{\mathbf{yp}}^{R\times I}$ is the transfer matrix that relates field pressures on the hologram and reconstruction surfaces.

The energetic sum (across the rows of $\mathbf{Y}'$) of all the reconstructed sound pressure levels (SPL) comprises the total M-SONAH reconstructed field. An example reconstruction at 125 Hz, over a horizontal plane at the nozzle centerline height is shown in Fig. 2(a). The reconstruction of the field shows a large main lobe radiating in a preferred aft direction. The local minimum running along $x = 3$ m is a destructive interference null due to the ground reflection. Such interference patterns were captured in both the physical measurement and in M-SONAH reconstruction due to incorporation of the reflecting plane into the field model. An M-SONAH reconstruction on a cylinder at the equivalent nozzle lip line, as shown as the solid line in Fig. 2(b), represents (or approximates) the frequency-dependent source distribution. The M-SONAH reconstruction is the first step in the OLVR process.

TABLE I. Sub-algorithms of OLVR and their steps.

NAH sound field reconstruction	*1. Perform SVD-based PFD of measured hologram data*
	2. Propagate each partial field using NAH
Selection of VR locations	*3. Select candidate VR locations*
	4. Calculate the MUSIC power for each candidate VR location
	5. Select VR locations with high MUSIC power and low total coherence
	6. Rearrange VRs in spatial order
Generation of partial fields using PCD	*7. Perform a Cholesky decomposition of the VRs.*
	8. Project sound field signals onto decomposed reference basis

B. Selection of VR locations

The second step in the OLVR process is to select VR locations. VRs can be placed anywhere in the NAH-reconstructed sound field, since the inclusion of multiple PFs preserves (or rather can be used to estimate) the cross-spectral information of the sound field. If the VRs are selected such that they are co-located with independent source regions, then they provide a means whereby the field can be decomposed into the contributions from these individual radiators. NAH reconstructions along the equivalent nozzle lip line of the jet are used to approximate the source. For the current implementation, VR locations were selected along this source region [e.g., see Fig. 2(b)].

The PFD experiment of Kim *et al.*[16] was successful in isolating the contributions of spatially distinct sources, but the technique was modified here to determine the optimal locations of VRs in the jet noise field where multiple sources are not as distinct. The candidate VR locations included all the data along the equivalent nozzle lip line at the height of the jet centerline. In describing the steps of this optimization process, the matrix $\mathbf{Y}^{N\times L}$ is the matrix $\mathbf{Y}'^{R\times L}$ limited to a subset of N candidate points.

The MUSIC algorithm is used to down-select the candidate locations to find an optimal set of VRs. The MUSIC power calculation depends on the noise subspace, which is estimated at all N locations. The cross-spectral matrix of the candidate VRs is calculated using all L terms for each reference vector in $\mathbf{Y}$ (i.e., the complex pressures of each partial field),

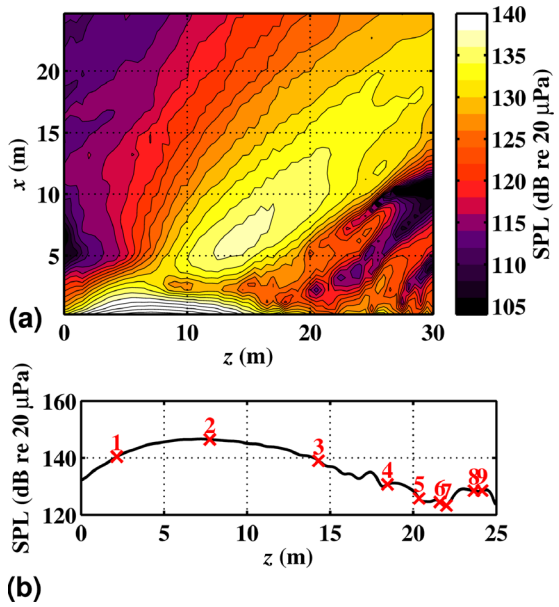

FIG. 2. (Color online.) M-SONAH total field reconstructions of the jet noise at 125 Hz. (a) Reconstruction over a planar region at a height $y = 1.9$ m above the ground. (b) Reconstruction at the equivalent nozzle lip line to represent the source. Symbols "x" mark the locations of the selected VRs.

$$\mathbf{S}_{\mathbf{yy}}^{N\times N} = \mathbf{Y}\mathbf{Y}^{\mathrm{H}}. \tag{2}$$

$\mathbf{S}_{\mathbf{yy}}^{N\times N}$ is decomposed using an SVD to obtain

$$\mathbf{S}_{\mathbf{yy}}^{N\times N} = \mathbf{W}\mathbf{\Sigma}\mathbf{W}^{\mathrm{H}}, \tag{3}$$

where the superscript H is the Hermitian transpose, and the diagonal elements of $\mathbf{\Sigma}^{N\times N}$ are the singular values. The unitary matrix, $\mathbf{W}^{N\times N}$, can be expressed in terms of singular vectors, i.e., $\mathbf{W} = [\mathbf{w}_1\ \mathbf{w}_2\ \cdots \mathbf{w}_N]$, where $\mathbf{w}_n^{N\times 1}$ is the nth singular vector associated with the nth singular value. If there are K independent sources that generate the field, then there are K source-related singular vectors and the noise subspace can be defined in terms of the noise-related vectors, $\mathbf{w}_n$, (for $n = K+1$ to N), as

$$\mathbf{R}_{\mathrm{noise}}^{N\times N} = \sum_{n=K+1}^{N} \mathbf{w}_n\mathbf{w}_n^{\mathrm{H}}. \tag{4}$$

In terms of a jet, the number of sources is ambiguous, characterized by a gradual decay of singular values.[30] The idea of a "source separation" may not exist for partially coherent sources, at least not with a unique solution. However, the value of K can generally be chosen in order to return a total field that approaches the measured energy within a desired precision using the virtual coherence method.[27] Limitations in the reference array[25] made such an approach difficult in this experiment, so K was chosen to be equal to the number of singular values contained in $\mathbf{\Sigma}$ that were within the *ad hoc* value of 40 dB from the maximum singular value. This resulted in $K = 11$ for 63 Hz, $K = 11$ for 125 Hz (the example case shown above), $K = 12$ for 250 Hz, and $K = 14$ for 500 Hz (see Sec. IV).

With the noise subspace estimated, the MUSIC powers are calculated at all locations. All of the singular vectors are orthogonal, so the subspace spanned by the source-related singular vectors, $\mathbf{w}_n$ ($n = 1$ to K), is orthogonal to the noise subspace. The calculation of the MUSIC powers relies on this fact. To obtain the MUSIC powers, it is first assumed that a source is located at the nth point within the candidate set of VRs, which is represented by a "trial vector,"

$$\mathbf{u}_n^{N\times 1} = [0\ \cdots 0\ 1\ 0\ \cdots 0]^{\mathrm{T}}, \tag{5}$$

where T is the matrix transpose. The nth element of $\mathbf{u}_n$ is unity, and all other $N-1$ elements are zero. The MUSIC power corresponding to the nth location is then calculated in terms of the trial vectors and the noise subspace as

$$P_{\mathrm{MUSIC}} = \frac{1}{\mathbf{u}^{\mathrm{H}}\mathbf{R}_{\mathrm{noise}}\mathbf{u}}. \tag{6}$$

Theoretically, the MUSIC power is infinite when $\mathbf{u}^{N\times 1} = \mathbf{w}_n^{N\times 1}$ for $n = 1$ to K, or in other words, when the trial vector represents an actual source distribution exactly. The calculation of the MUSIC power is repeated for all N candidate VR locations, and higher values of MUSIC power indicate locations that contain larger portions of self-coherent field energy, or the most likely spatial location of a source.

Multiple locations near a distributed source can be "good" VR locations, and thus return high MUSIC powers. Kim *et al.*[16] recommend that the redundant VRs, characterized by large mutual coherence, be removed, leaving only the one with highest MUSIC power for each source. This process is straightforward in the case of spatially distinct sources. However, in the jet noise field, the spatial coherence is characterized by gradual changes and no clear source distinctions. Hence, an algorithm for the removal of redundant references that accounts for partial spatial coherence has been developed.

The removal of redundant VRs begins by placing VRs at *all* N candidate reconstruction locations and sorting them according to their respective MUSIC power to obtain $\mathbf{X}'^{N\times L}$, which contains the same N reference vectors in $\mathbf{Y}$, but reordered. Then, from the candidate VR cross-spectral matrix, $\mathbf{S}_{\mathbf{x}'\mathbf{x}'}^{N\times N} = \mathbf{X}'\mathbf{X}'^{\mathrm{H}}$, the coherence between all locations i and j is calculated as

$$\gamma_{ij}^2 = \frac{|S_{ij}|^2}{S_{ii}S_{jj}}, \tag{7}$$

where S_{ii} and S_{jj} are the autospectra of references i and j, respectively, and S_{ij} is the cross spectrum between the two. The first VR, which has the highest MUSIC power, is selected as the first VR for the final, optimized set. The candidates VRs are then searched in descending order of MUSIC power until a second VR is found whose coherence with the first VR falls below a certain threshold. This second VR is also selected for the final set. All candidates between these two are considered redundant and removed from the set. This process continues to find the third VR of high MUSIC power whose coherence with the first and second is below the same threshold, and so on to the end of the set of candidates. The coherence threshold is chosen independently

for each frequency such that the number of final VRs is equal to K. This resulted in a coherence threshold of 0.44 for 63 Hz, 0.31 for 125 Hz, 0.21 for 250 Hz, and 0.17 for 500 Hz. The resulting set of K VRs is sorted in order of highest to lowest MUSIC powers, and mutual coherence below the chosen threshold.

The final step of the VR selection process is to reorder the final VR set spatially, with respect to distance from the nozzle. The order of the VRs influences the resulting PFs, but does not change the fact that the PF set results from an optimized VR selection process. Spatial ordering is found to produce partial sources that are more amenable to analytical wavepacket modeling than partial sources produced without VR reordering, as discussed in Sec. V A. The numbered markers on Fig. 2(b) show the locations of the first 9 (of $K = 11$ total) VRs for the 125 Hz case. Note that the VR pairs 6-7 and 8-9 each have elements separated by less than 1 m, which demonstrates the relatively low spatial coherence of the low-amplitude region. The downstream source region containing these VRs, as well as 10 and 11, may be dominated by the incoherent noise floor of the field.

The final VR matrix consists of the set of complex pressure values at the selected VR locations,

$$\mathbf{X}^{K\times L} = \begin{bmatrix} \mathbf{Y}_{R_1} \\ \mathbf{Y}_{R_2} \\ \vdots \\ \mathbf{Y}_{R_k} \\ \vdots \\ \mathbf{Y}_{R_K} \end{bmatrix}, \tag{8}$$

where $\mathbf{Y}_{R_k}$ represents the R_kth row of $\mathbf{Y}^{N\times L}$, and R_k is the corresponding index of the kth VR from the final set.

C. Generation of partial fields

With VRs selected, $\mathbf{X}^{K\times L}$ is decomposed to form a linearly independent basis set corresponding to the independent sources. This was performed with the PCD method, which iteratively allocates and removes energy from the VR cross-spectral matrix. A mathematical derivation of the PCD technique is provided by Bendat.[28] Hallman and Bolton,[31] and Kwon and Bolton[32] provided comparisons of SVD-based PFD (sometimes called the "virtual coherence" method) and PCD. Here, a Cholesky decomposition of the complex pressures of the VRs was used to perform the PCD, represented by

$$\mathbf{S}_{\mathbf{xx}}^{K\times K} = \mathbf{X}\mathbf{X}^{\mathrm{H}} = \mathbf{L}\mathbf{L}^{\mathrm{H}}, \tag{9}$$

where $\mathbf{L}^{K\times K}$ is a lower triangular matrix containing the now linearly independent basis vectors. In essence, all information in the VR set that was coherent with the first reference is combined in the first basis vector, or the first column of $\mathbf{L}$. This information is then removed from the cross-spectral matrix $\mathbf{S}_{\mathbf{xx}}^{K\times K}$. All remaining information that is coherent with the second VR is then removed from the set, and so on.

The magnitudes $[10\log_{10}(|\cdot|^2/(20\,\mu\mathrm{Pa})^2)]$ of the elements of $\mathbf{L}$, from the Cholesky decomposition of $\mathbf{S}_{\mathbf{xx}}^{K\times K}$ in Eq. (9), are shown in Fig. 3 for the 125-Hz case. Their linear independence is reflected by the triangular nature of the matrix. The relative magnitudes of the vector elements when compared across VRs gives a general indication of the relative strengths of the corresponding OLVR PFs that will be generated. For example, the highest levels in VRs 1–3 are 12 dB higher than VRs 4 and beyond.

Finally, the OLVR PFs are generated from the basis set of the new, decomposed VRs. The cross spectral matrix between all M field points and the K VRs is calculated as

$$\mathbf{S}_{\mathbf{xy}}^{K\times M} = \mathbf{X}\mathbf{Y}^{\mathrm{H}}. \tag{10}$$

The OLVR partial fields are obtained with

$$\mathbf{P}_{\mathbf{x}}^{M\times K} = \mathbf{S}_{\mathbf{xy}}^{\mathrm{H}}(\mathbf{L}^{\mathrm{H}})^{-1}. \tag{11}$$

Because of the optimized, coherence-based selection of the VRs, the resulting OLVR PFs each contain radiation energy that is coherent with a single localized point along the jet noise source region.

IV. OLVR RESULTS AND DISCUSSION

A. Source decompositions

The OLVR process described in Sec. III is performed at select frequencies: 63, 125, 250, and 500 Hz. The jet engine, operating at 100% ETR, has a noise spectral peak frequency of approximately 250 Hz in the maximum radiation direction.[26] Thus, the selected frequencies fall below, at, and above the spectral peak—and based on prior intensity,[33] holography,[25] and beamforming[34] analyses, span a critical source transition region for the jet. This subsection shows the resulting OLVR partial fields along the equivalent nozzle lip line, or the *partial sources*. In this paper, the terms "partial source" and "source" are used to simplify discussion and to designate, respectively, OLVR decomposed and total (summed) pressures along the nozzle lip line, whereas other jet publications may define equivalent source regions differently. The abbreviation PF can be used to designate or

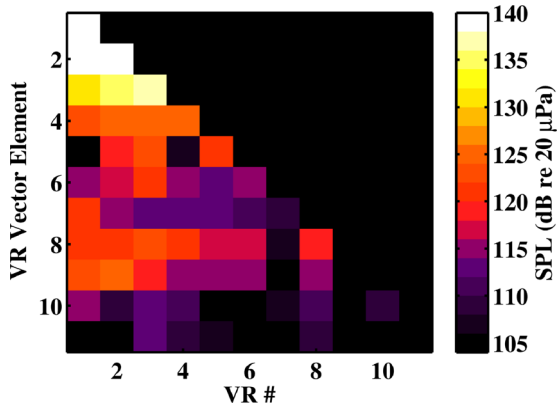

FIG. 3. (Color online.) Matrix $\mathbf{L}$ levels after Cholesky decomposition, for the 125-Hz example case.

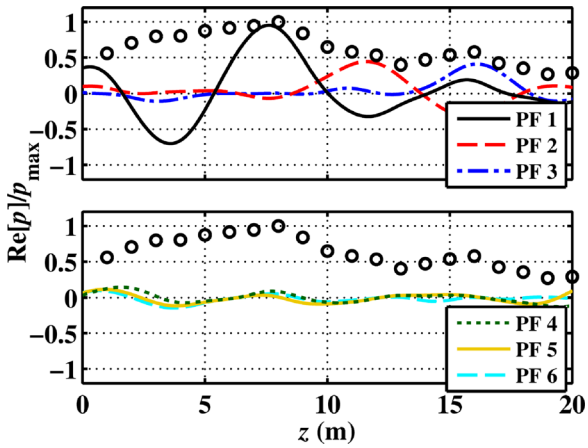

FIG. 4. (Color online.) Real parts of PFs 1–6 (lines) and total rms pressure (circles) along the nozzle lip line for 63 Hz.

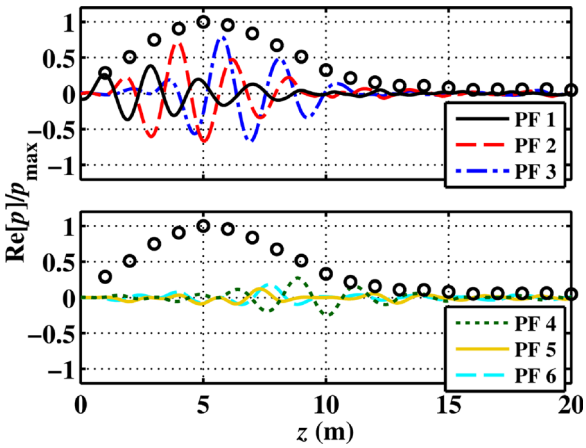

FIG. 6. (Color online.) Real parts of PFs 1–6 (lines) and total rms pressure (circles) along the nozzle lip line for 250 Hz.

identify the sequential number (e.g., "PF 2") of either partial source pressures or partial field pressures at locations other than the nozzle lip line.

Physical insights can be drawn from the OLVR PF representation of the jet noise sources and field. It is important to note that many of these insights cannot be obtained directly from physical jet noise measurements based on simple arrays, such as polar arcs in the far field—high resolution, near-field measurements, and analyses are required.

The OLVR partial sources for the selected frequencies (Figs. 4–7) give insights into the frequency-dependent nature of jet noise sources. For each frequency, the two subfigures show PFs 1–3 (upper) and PFs 4–6 (lower) for clarity. The root-mean-square (rms) pressures of the total field reconstructed at the nozzle lip line, normalized by the maximum at that frequency, are shown by circles. Normalization has removed information about the frequency-dependent source levels, but this information can be found in the spatial/spectral data of Ref. 25. Real parts of the complex pressure values of the sources are shown by lines. Inclusion of a forward progression in time would result in traveling waves moving in the direction of increasing z, bounded by each PFs respective spatial envelope frozen in the time domain. The PFs demonstrate the characteristic wavelengths, distributions, and fluctuating behaviors of each partial source.

Most partial sources are characterized by monotonic growth, saturation, and monotonic decay as a function of z. A comparison of the total field distributions across Figs. 4–7 suggests that the total source distributions contract and move upstream as frequency is increased from 63 to 500 Hz. (Note that some of the downstream energy, past $z \approx 10$ m, may be missing from the total source reconstruction due to the limited aperture of the NAH array as explained in Ref. 25. This fact may have some influence on the distributions of the PFs.) More interestingly, this behavior is largely mimicked by each respective partial source across the same frequencies, e.g., PF 3 has a magnitude maximum near $z = 17$, 12, 6, and 3 m for 63, 125, 250, and 500 Hz, respectively. The narrowing of source distributions with an increase in frequency occurs for both total and partial sources in a similar manner.

A consequence of the partially coherent nature of the source is that the PF distributions tend to overlap, even though their respective maxima are spatially distinct, and the degree to which this overlap occurs depends on frequency. For example, PFs 1, 2, and 3 at 125 Hz have more similar

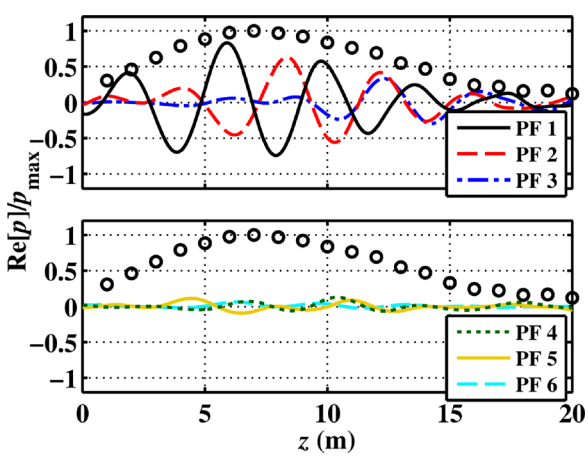

FIG. 5. (Color online.) Real parts of PFs 1–6 (lines) and total rms pressure (circles) along the nozzle lip line for 125 Hz.

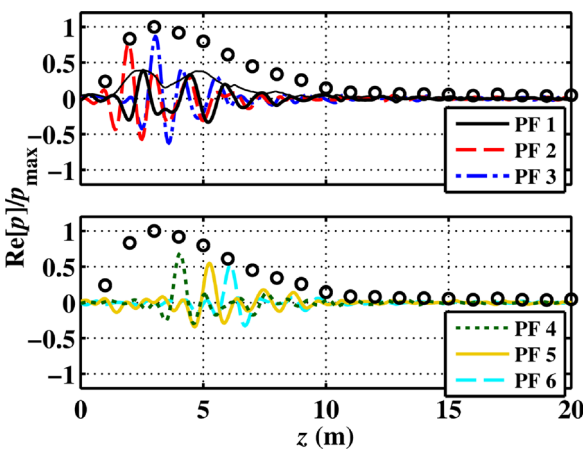

FIG. 7. (Color online.) Real parts of PFs 1–6 (thick lines) and total rms pressure (circles) along the nozzle lip line for 500 Hz. The thinner solid line shows the envelope (absolute value) of PF 1.

magnitudes across the regions of their respective maxima ($z = 6$ to 15 m in Fig. 5), than do PFs 2, 3, 4, 5, and 6 of the 500-Hz case ($z = 2$ to 7 m in Fig. 7) whose distributions decay more rapidly as they approach the maximum locations of their nearest neighboring PFs. The VR selection method requires further investigation to understand how VR spacing might affect the PF distributions, but it is clear that frequency-dependent spatial coherence has a critical effect on jet noise source characterization.

A direct consequence of the spatial ordering of VRs as explained in Sec. III B is that the partial sources tend to be spatially ordered. For example, the dominant PFs at 63 Hz have maxima that are ordered PFs 1, 2, and 3 from nozzle to downstream. Similarly, PF maxima for both 125 and 250 Hz are ordered PFs 1, 2, 3, and 4. This is a property that cannot be obtained from SVD-based PFD methods. Exceptions to this trend occur, the strongest of which is PF 1 in the 500-Hz case in Fig. 7. The envelope (absolute value) of PF 1 is included (thin solid line) to clarify the precise locations of the local maxima. The envelope shows two local maxima at about $z = 2.5$ and 5 m (farther downstream than the maxima of other PFs), even though its VR is located at $z = 0$ m. (The remaining PFs 2–6 are still ordered spatially.) This occurs because there exists some low-amplitude source information near the nozzle that is coherent with higher-amplitude energy farther downstream, a property that cannot be explained by jet mixing noise sources alone. The passage of turbulent structures through regularly-spaced shock cells is suggested as a potential cause,[18] and indeed coherent upstream and downstream radiation was demonstrated for broadband shock-associated noise from a full-scale jet in Ref. 35. This hypothesis could be more thoroughly investigated by expanding OLVR PFD analyses to more frequencies that span jet noise sources containing broadband shock-associated noise, and could be confirmed through simultaneous fluid-flow and acoustic imaging.

Another consequence of the spatial ordering of the VRs is that PF 1 does not necessarily contain the dominant field energy, as is always the case in SVD-based methods. A comparison of the total source maxima in Figs. 4–7 to the relative PF magnitudes at those maximum locations reveals that PF 1 does dominate the source for 63 and 125 Hz, but the 250-Hz source is dominated by PF 2 and the 500-Hz source by PF 3. In general, the most energetic partial sources are those whose maxima fall in the region of the total source maximum.

B. Field decompositions

This subsection presents some of the OLVR partial field radiation properties related to the 100% ETR partial source information discussed in Sec. IV A. Far-field pressures along a polar arc (see Fig. 1) that correspond to the same partial sources above are shown in Figs. 8–11 for the frequencies of 63, 125, 250, and 500 Hz, respectively. These reconstructions are at a height of $y = 1.9$ m, at a radius of 23 m from an estimated maximum-source region 5.5 m downstream of the nozzle, and are shown as a function of polar directivity angle θ, relative to the inlet. Similar to the source results, each

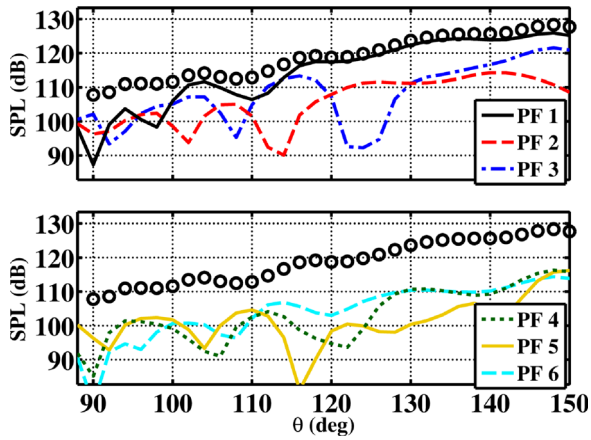

FIG. 8. (Color online.) Energetic summation of all $K = 12$ PFs (circles) and the first six individual PFs (lines) at height $y = 1.9$ m, radius 23 m, as a function of polar angle re inlet, for 63 Hz.

figure here is separated into two subfigures showing PFs 1–3 and PFs 4–6 for clarity. The total reconstructed field levels (dB re 20 μPa) are shown by circles and the levels of each partial field are shown by lines. These far-field levels demonstrate the characteristic directivities of each partial source and the relative contributions of each partial source to the radiated field as a function of angle.

A comparison of the OLVR PFs with dominant field energies in Figs. 8–11 to the dominant source energies in Figs. 4–7 shows that the PFs with largest amplitudes near the total source maxima tend to produce the highest levels in the far-field regions of maximum radiation. For example, at 63 Hz, PF 1 is the dominant source around $z = 7.5$ m in Fig. 4 and produces the highest levels by at least 4 dB toward 150° in Fig. 8. For the 125-Hz case, PFs 1 and 2 show relatively similar pressure values (a 20% difference in respective maxima) in Fig. 5 near $z = 7$ m and a mere 1 dB difference in the maximum radiation direction of 142° in Fig. 9. PFs 2 and 3 dominate both source and field in Figs. 6 and 10.

The 500 Hz data present an interesting case again; all six PFs shown have source pressure maxima within a 50% range in Fig. 7. Although PF 3 clearly dominates the local

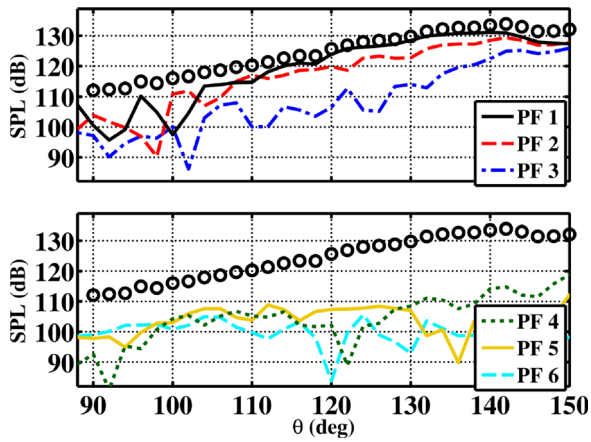

FIG. 9. (Color online.) Energetic summation of all $K = 11$ PFs (circles) and the first six individual PFs (lines) at height $y = 1.9$ m, radius 23 m, as a function of polar angle re inlet, for 125 Hz.

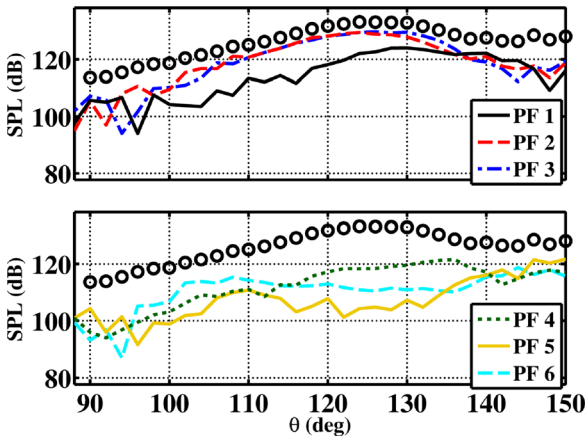

FIG. 10. (Color online.) Energetic summation of all $K = 12$ PFs (circles) and the first six individual PFs (lines) at height $y = 1.9$ m, radius 23 m, as a function of polar angle re inlet, for 250 Hz.

source maximum at $z = 3$ m and the field maximum at $\theta = 122°$, there is only a 6 dB spread of all six maximum PF values in the Fig. 11 directivities when all angles are considered. Contrast this to the 11 dB spread in PF directivity maxima for 250 Hz, and even more for the two lower frequencies. This strengthens the argument that a higher number of partial fields are generally required to characterize jet noise sources of higher frequencies. Overall, the total field levels in Fig. 11 appear to receive significant contributions from all six PFs (as well as higher PFs not shown) across most angles, because the 500-Hz PFs are more similar in level than the PFs for the three lower frequencies. The compact partial sources at 500 Hz are not omnidirectional, but they radiate broader lobes with more angular overlap than do the lower-frequency sources.

V. REDUCED-ORDER MODELING OF TACTICAL AIRCRAFT NOISE

Some previous studies seeking to predict or model jet noise radiation have used only 1–3 source terms per frequency, or "modes," that capture the majority of the total radiated energy.[15,36,37] Such "reduced-order" models tend to be successful in reproducing far-field levels in the dominant radiation direction. However, even the reduced-order models that incorporate a source term focused on predicting sideline levels may not provide a complete description of the jet noise field if the finite spatial coherence[34,35,38] is excluded from the model. The inclusion of higher-order terms can be used to improve both level and coherence predictions in all radiation directions (not just in the primary aft lobe).

Like the partial fields resulting from different PFD algorithms, the inclusion of both low-order and higher-order terms in a source model is a nonunique process. The problem with higher-order partial sources from SVD-based methods is that they tend to have complicated distributions (shapes) that are difficult to model analytically. They may also be difficult to isolate from the measurement noise floor because of their relatively low amplitudes compared to the lower-order source terms. The OLVR partial fields discussed here overcome these two challenges.

In this section, a demonstration of the effects of low-order modeling is made by comparing the jet noise field prediction using only three OLVR PF terms to the full-field prediction with all PFs. Then, an analytical wavepacket model is produced directly from the full set of OLVR partial sources at multiple frequencies to show their potential as an input for higher-order jet noise modeling.

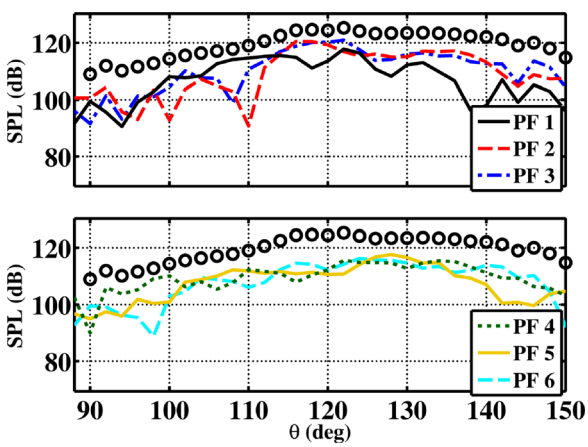

FIG. 11. (Color online.) Energetic summation of all $K = 14$ PFs (circles) and the first six individual PFs (lines) at height $y = 1.9$ m, radius 23 m, as a function of polar angle re inlet, for 500 Hz.

A. Low-order representation vs full-field representation

The idea that the main radiation lobe of a tactical aircraft jet engine can be represented by 1 or 2 PFs for some frequencies, whereas many more are required to represent the total radiated field away from the main lobe, is an important finding (see Sec. IV B). The results here are an independent verification of the similarity spectra analysis of Neilsen *et al.*,[39] where the measured spectra at the ground reference array were decomposed into the large and fine-scale similarity spectra developed by Tam *et al.*[40] For the same engine condition shown in this paper, the Neilsen *et al.* fine-scale spectrum was found to be present at angles of 110° and less, and was solely responsible for the radiation from 90° forward. This corroborates the results for 63 and 125 Hz, shown in Figs. 8 and 9, respectively, where the total field summation is well represented (dominated) by 1 or 2 PFs, but only for about 110° and aft.

As one detailed demonstration of the angular dependence of required partial fields in a reduced-order model, consider field reconstructions at 125 Hz over the 30 m × 25 m aperture (at height $y = 1.9$ m). The reconstructed field based on only the first three (most energetic) PFs, shown in Fig. 12(a), can be compared with the total predicted field obtained with all 11 PFs in Fig. 12(b). The difference between the two predictions in Fig. 12(c) yields a decibel error for the reduced-order source representation as a function of location. Although three PFs are sufficient to capture 97% of the total field energy, and all the energy in the maximum radiation lobe, the error between the full-field and reduced-order predictions is indeed significant along a localized angular span forward of about 110°. Thus, reduced-order modeling that neglects to describe this

angular region will be unable to adequately capture the radiated sideline energy. Adequate modeling of this sideline radiation is important from a hearing conservation perspective, as aircraft ground support personnel are often located in this region during post-maintenance run-ups and preflight tests.

B. Analytical wavepacket modeling

An analytical representation that describes the dominant jet noise radiation with sufficient accuracy from a high-performance engine is of significant utility for at least two reasons. First, an analytical model greatly simplifies the noise prediction problem by reducing computational complexity. Second, an analytical "wavepacket" model ties the present work to the laboratory-scale and numerical branches of the jet noise community, where wavepacket analyses have been numerous. The OLVR-based partial sources described here have characteristics that suggest they can be modeled with analytical pressure wavepackets, with the number of wavepackets required increasing with frequency and at the sideline.

Wavepacket representations of jet noise strive to provide a model consistent with linear stability theory of the mean flow[41,42] that incorporates features of the highly directional turbulent mixing noise.[15,43,44] A wavepacket has been described as a spatially extended source characterized by an axial amplitude distribution that grows, saturates, and decays; an axial phase relationship that produces directional noise;[38] and correlation lengths longer than the integral length scales of the turbulence.[45] These wavepacket analyses are often sought to represent the dominant PFD (i.e., POD) modes or other salient jet noise source features. For example, Reba *et al.*[38] used a Gaussian wavepacket model to represent large turbulent structures, and fitted their model to measurements made in the hydrodynamic regime. They incorporated the measured effects of spatially varying amplitude, phase, and coherence. Schlinker *et al.*[37] used a parabolized stability equation ansatz to educe wavepacket parameters from measurements made in the hydrodynamic near field.

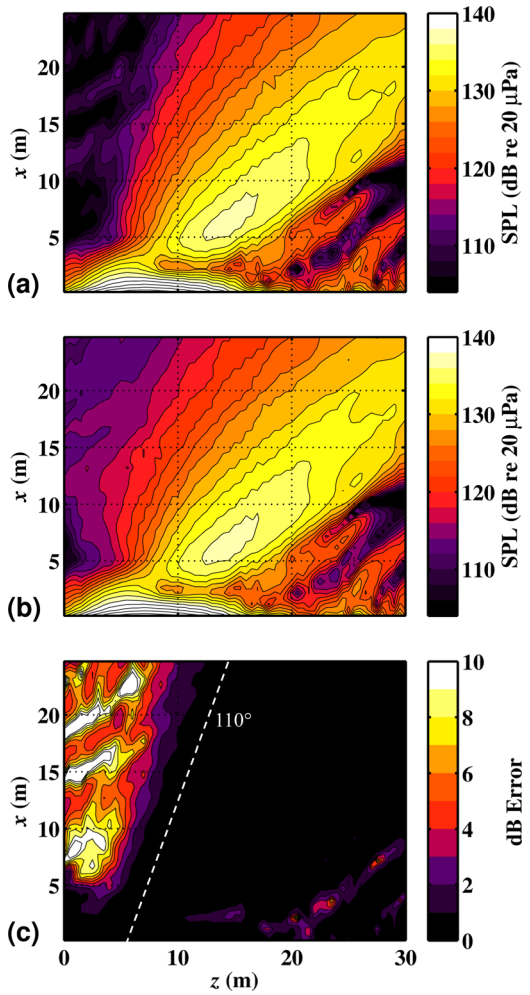

FIG. 12. (Color online.) Reduced-order vs higher-order representation of sound field at 125 Hz. (a) Energetic sum of PFs 1–3. (b) Sum of all PFs. (c) Absolute value of the SPL difference.

Measurements made outside the hydrodynamic field are also useful in understanding equivalent source characteristics. Kœnig *et al.*[46] employed a spatial PFD and temporal wavelet transforms of jet noise measured on a polar arc array and showed that both approaches lead to coherent structures with directivity in agreement with a wavepacket model. Morris[47] used the decomposition of far-field spectra to obtain frequency-dependent, axial wavenumber spectra corresponding to the large-scale turbulent mixing noise. Papamoschou[36,48] used an analytical, single-wavepacket model plus a monopole to predict far-field sound levels. Neilsen *et al.*[49] extended these approaches to obtain frequency-dependent wavepackets for large-scale turbulent mixing noise and an uncorrelated source distribution to account for the fine-scale turbulent mixing noise of a Mach 1.8 laboratory-scale jet. In related full-scale work, Neilsen *et al.*[50] and Harker *et al.*[34] have pursued approaches to extracting wavepacket models from linear microphone arrays that span the source region.

The OLVR partial sources can be matched to an analytical wavepackets ansatz. A six-parameter asymmetric Gaussian wavepacket for the nozzle lip line pressure is employed. The candidate wavepacket model is

$$p_0(z) = Ae^{-b(z)\{z-z_0\}^2} e^{i(\alpha z+\phi)}, \tag{12}$$

where

$$b(z) = \begin{cases} b_1 & z < z0, \\ b_2 & z > z0. \end{cases} \tag{13}$$

In Eqs. (12) and (13), the parameters A, b_1, b_2, and z_0 define the wavepacket envelope, whereas α represents a constant phase gradient along z that gives rise to directional radiation.

The advantage of this simple analytical wavepacket model is that these parameters come directly from the amplitude, phase, and wavenumber spectrum of a given OLVR partial source. The maximum pressure amplitude of the partial source is chosen as A, and its location is selected as z_0. The growth and decay parameters, b_1 and b_2, are determined by picking some fraction $(1/d)$ of the maximum amplitude, and locating the corresponding point, z_i, where the amplitude is equal to A/d,

$$\frac{A}{d} = |p(z_i)| = Ae^{-b_i(z_i-z_0)^2}. \tag{14}$$

Now each b can be solved for explicitly in terms of the chosen d (equal to 2 for this paper) and corresponding z values,

$$b_i = -(z_i - z_0)^{-2} \ln(1/d). \tag{15}$$

For partial sources containing multiple local maxima, such as PF 1 at 500 Hz (see Fig. 7), multiple values of z_i were sometimes discovered to meet the criteria of Eq. (14). In such cases, the selection of z_i closest to z_0 was enforced. The convective wavenumber, α, in the wavepacket model is selected to be the peak in the OLVR partial source wavenumber spectrum, similar to the approach by Morris[47] and Neilsen *et al.*[49,50] The spatial Fourier transform of the partial field is taken to find the wavenumber spectrum. The parameter, ϕ, accounts for any residual constant phase offset between the partial field and the wavepacket once α has been selected; it is computed by the mean of the difference in unwrapped phases of the wavepacket and partial field in a small region around z_0. In this way, the OLVR partial sources are each modeled as wavepackets.

Examples of the OLVR-based wavepackets are given for the 125 Hz case. Specifically, the real parts of the fitted wavepackets (Re{WP}) are compared to the real parts of the first six OLVR partial sources (Re{PF}), which are displayed as solid lines in Fig. 13. The dashed lines are the magnitude of the complex pressures (|WP| and |PF|). Note how the asymmetric Gaussian shape is able to track the salient features of the wavepacket—both the amplitude envelope and the rate of oscillation—for the first three OLVR partial sources that form the overall source region. However, a problem arises for partial fields that do not follow a traditional wavepacket shape. In partial sources 4–6, which are of appreciably lower energy, there are secondary local maxima and other features that this analytical wavepacket fitting is unable to capture. While small, these deviations of the higher order partial sources from smooth wavepacket-like behavior add complexity to the radiated field and could indicate extended spatially coherent source components that are difficult to fully match with wavepackets modeled as asymmetric Gaussian analytical functions.

The simplicity of these wavepackets is of great worth. Since each parameter has an analytical solution, the fitting process is quick and robust, and the entirety of each wavepacket is reduced to six parameters. Figure 14 shows a comparison between all K wavepackets (WP) and partial sources (PF), along with the respective energetic summations of each (PF sum and WP sum) for the four frequencies shown previously. Magnitudes have been normalized according to the total source maxima. The wavepackets and their summations at 63, 125, and 250 Hz match the partial sources well, because the most energetic partial sources at these frequencies are characterized by monotonic growth and decay. While this agreement may seem trivial, it confirms that the OLVR decompositions performed in this paper produce physically meaningful partial sources for jet noise based on

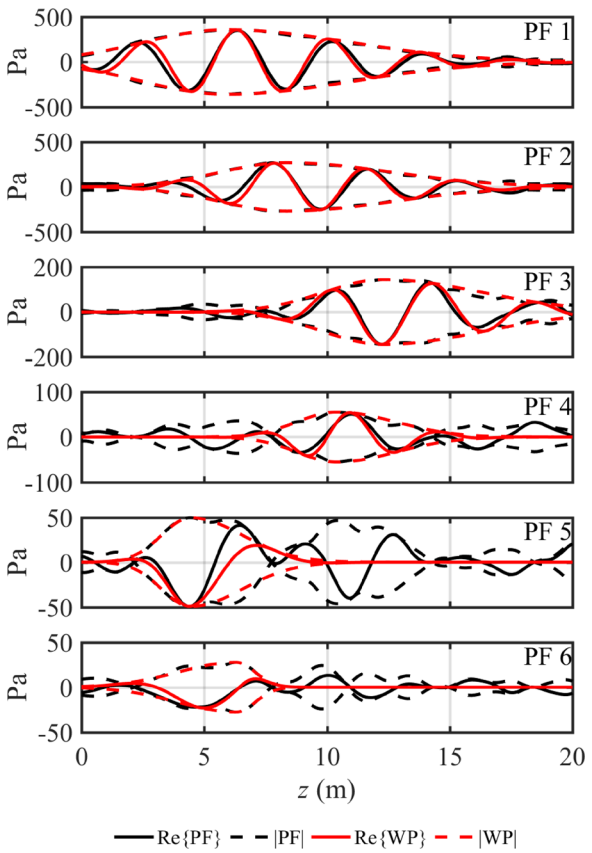

FIG. 13. (Color online.) Partial sources, Re{PF}, with corresponding fitted wavepackets, Re{WP}, at 125 Hz. The magnitude of the pressures, |PF| and |WP|, are given by the dashed lines.

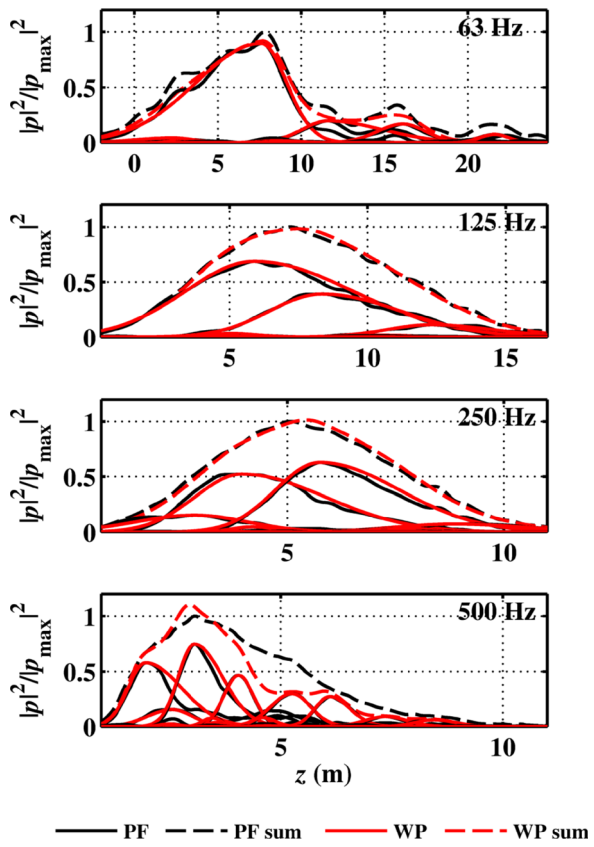

FIG. 14. (Color online.) Comparison of fitted wavepacket magnitudes (WP) to their respective partial sources (PF). Dashed lines are the energetic summation of all wavepackets (WP sum) to the summation of all partial sources (PF sum).

spatial coherence at the source; this is only the second attempt ever to perform a complex wavepacket source analysis of a full-scale, high-performance tactical aircraft (see Ref. 34 for the first). The best verification for a wavepacket model is the projection of the derived sources into the field, and such an analysis will be demonstrated in subsequent publications.

At 500 Hz in Fig. 14, where all wavepackets contribute significantly to the total source region, the overall agreement between wavepackets and partial sources is not as exact due to the secondary local maxima downstream in the PFs (or relatively high spatial coherence) that are not represented by the wavepackets (e.g., see partial source PF 1 for 500 Hz in Fig. 7). These discrepancies cause the wavepacket sum to miss a significant amount of energy between around $z = 4$ and 8 m. In the end, however, the OLVR method is able to provide a simple means of analytically representing independent, equivalent acoustic source contributions below, at, and above the peak-frequency regime of the noise radiation.

VI. CONCLUDING DISCUSSION

Targeted identification and isolation of noise sources through high-resolution acoustic imaging and PFD can be used to inform jet noise reduction technologies in ways that more basic measurements of field noise levels cannot. Although PFD is a nonunique process, a thorough understanding of the bases onto which the field is projected (decomposed) can lead to physical source insights. The OLVR method relies on physically intuitive basis signals that reflect the spatial coherence properties of the field. In the OLVR implementation shown here, virtual references (extracted from NAH field reconstructions along the nozzle lip line) were selected along the extent of a jet source region such that there was low coherence among the reference signals, yet high MUSIC power (significant source information) in each one independently. Spatial ordering of the reference signals prior to decomposition resulted in partial fields whose maxima were distinct and nominally spatially ordered, and that were often characterized by monotonic growth, saturation, and decay.

Key physical insights for full-scale jet noise at 100% ETR from the OLVR partial sources include the fact that the partial coherence of both the source and the field are frequency dependent. Well-understood features of equivalent acoustic jet noise models, such as becoming more compact and shifting upstream with increasing frequency, were largely mimicked by the partial sources, a direct manifestation of the decreasing source coherence with frequency. It was shown that low spatial coherence forward of the main radiation lobe (even for frequencies at and below the peak frequency) and decreasing coherence with increasing frequency require a higher number of significant (high-energy) partial sources to describe the full radiated field.

One of the most interesting physical insights comes from the OLVR partial sources that did not follow the trends of monotonic growth and decay around a single maximum—some partial sources, most notably at the highest frequency shown (500 Hz), were characterized by multiple local maxima far away from their respective virtual reference location. The reason for this anomaly requires further investigation, but it is hypothesized to be due to the interaction of turbulent features with spatially distinct shock cells that generates broadband shock-associated noise radiating both upstream and downstream, as confirmed in other studies.[18,35] It is important to note that many of the detailed source analyses performed here were made possible by the physically meaningful OLVR decomposition and would not be attainable from conventional SVD-based methods. The advantage of OLVR field decomposition and resulting partial sources is its ability to probe, isolate, and quantify physically relevant field features and equivalent source characteristics.

After the investigation of jet noise source and radiation phenomena captured by the OLVR partial fields, an analytical wavepacket model was obtained by fitting asymmetric Gaussian functions to each partial source independently. The shapes of the OLVR sound field distributions near the source region make these fields more amenable to wavepacket modeling than partial fields obtained from other PFD methods, allowing the inclusion of multiple mutually independent sources. The six parameters of the wavepacket model were calculated directly from the partial source distributions rather than requiring an optimized curve-fitting algorithm. Other than the cases where partial sources contained significant secondary local maxima, the summed wavepackets were shown to represent the total source distributions well. To predict sound radiation in the maximum region, only 1 or 2 PF-based wavepackets are required due to the high field coherence, but sideline and forward radiation requires more. This represents a practical approach to developing a frequency-dependent, wavepacket model for the spatially dependent sound radiation from high-performance military aircraft noise, which can be used for noise predictions and to investigate proposed noise reduction technologies.

ACKNOWLEDGMENTS

The authors gratefully acknowledge funding from the U.S. Air Force Research Laboratory (USAFRL) through the SBIR program and support through a Cooperative Research and Development Agreement between Blue Ridge Research and Consulting, Brigham Young University, and the Air Force; and from the Office of Naval Research. This research was supported in part by the appointment of A.T.W. to the Postgraduate Research Participation Program at the U.S. Air Force Research Laboratory, 711th Human Performance Wing, Human Effectiveness Directorate, Warfighter Interface Division, Battlespace Acoustics Branch administered by the Oak Ridge Institute for Science and Education through an interagency agreement between the U.S. Department of Energy and USAFRL.

[1]R. E. A. Arndt, D. F. Long, and M. N. Glauser, "The proper orthogonal decomposition of pressure fluctuations surrounding a turbulent jet," J. Fluid Mech. **340**, 1–33 (1997).
[2]C. E. Tinney, P. Jordan, J. Delville, A. M. Hall, and M. N. Glauser, "A time-resolved estimate of the turbulence and source mechanisms in a subsonic jet flow," AIAA Paper 2006-621 (2006).
[3]H. Vold, P. Shah, P. Morris, Y. Du, and D. Papamoschou, "Axisymmetry and azimuthal modes in jet noise," AIAA Paper 2012-2214 (2012).

[4]B. M. Harker, K. L. Gee, T. B. Neilsen, A. T. Wall, and M. M. James, "Wavepacket modeling and full-scale military jet noise beamforming analyses," AIAA Paper 2016-2129 (2016).
[5]J. Liu, A. Corrigan, K. Kailansanath, N. Heeb, and E. Gutmark, "Numerical study of noise characteristics in overexpanded jet flows," AIAA Paper 2015-0508 (2015).
[6]J. L. Lumley, "The structure of inhomogeneous turbulent flows," in *Atmospheric Turbulence and Radio Wave Propagation*, edited by A. M. Yaglom and V. I. Tatarsky (Publishing House Nauka, Moscow, USSR, 1967), pp. 166–176.
[7]M. Glauser and W. George, "Orthogonal decomposition of the axisymmetric jet mixing layer including azimuthal dependence," in *Advances in Turbulence* (Springer, Berlin, 1987), pp. 357–366.
[8]D. Long, T. van Lent, and R. Arndt, "Jet noise at low reynolds number," in *Proceedings of AIAA, Astrodynamics Specialist Conference* (1981).
[9]M. Lee and J. S. Bolton, "Source characterization of a subsonic jet by using near-field acoustical holography," J. Acoust. Soc. Am. **121**, 967–977 (2007).
[10]J. Freund and T. Colonius, "Turbulence and sound-field POD analysis of a turbulent jet," Int. J. Aeroacoust. **8**, 337–354 (2009).
[11]A. Towne, T. Colonius, P. Jordan, A. Cavalieri, and G. A. Brès, "Stochastic and nonlinear forcing of wavepackets in a Mach 0.9 jet," AIAA Paper 2015-2217 (2015).
[12]Z. P. Berger, M. G. Berry, P. R. Shea, M. N. Glauser, P. Kan, J. Lewalle, C. J. Ruscher, and S. Gogineni, "Investigation of 'loud' modes in a high-speed jet to identify noise-producing events," AIAA Paper 2015-0739 (2015).
[13]A. Sinha, D. Rodríguez, G. A. Brès, and T. Colonius, "Wavepacket models for supersonic jet noise," J. Fluid Mech. **742**, 71–95 (2014).
[14]Y. Du and P. J. Morris, "The separation of radiating and non-radiating near-field pressure fluctuations in supersonic jets," J. Sound Vib. **355**, 172–187 (2015).
[15]P. Jordan and T. Colonius, "Wave packets and turbulent jet noise," Annu. Rev. Fluid Mech. **45**, 173–195 (2013).
[16]Y. J. Kim, J. S. Bolton, and H. S. Kwon, "Partial sound field decomposition in multireference near-field acoustical holography by using optimally located virtual references," J. Acoust. Soc. Am. **115**, 1641–1652 (2004).
[17]D. M. Photiadis, "The relationship of singular value decomposition to wave-vector filtering in sound radiation problems," J. Acoust. Soc. Am. **88**, 1152–1159 (1990).
[18]A. T. Wall, K. L. Gee, T. B. Neilsen, and M. M. James, "Partial field decomposition of jet noise sources using optimally located virtual reference microphones," Proc. Mtgs. Acoust. **18**, 045001 (2012).
[19]D. H. Johnson and D. E. Dudgeon, *Array Signal Processing: Concepts and Techniques* (Prentice-Hall, Upper Saddle River, NJ, 1993).
[20]A. T. Wall, K. L. Gee, T. B. Neilsen, and M. M. James, "Acoustical holography and proper orthogonal decomposition methods for the analysis of military jet noise," in *Proceedings of Noise-Con 2013*, Denver, CO (2013).
[21]J. Hald, "STSF—A unique technique for scan-based nearfield acoustical holography without restriction on coherence," Technical Report No. 1, from Bruel & Kjaer, Naerum, Denmark, 1989.
[22]K.-U. Nam and Y.-H. Kim, "Visualization of multiple incoherent sources by the backward prediction of near-field acoustic holography," J. Acoust. Soc. Am. **109**, 1808–1816 (2001).
[23]S. M. Price and R. J. Bernhard, "Virtual coherence: A digital signal processing technique for incoherent source idientification," in *Proceedings of the 4th International Modal Analysis Conference* (1986), pp. 1256–1262.
[24]A. T. Wall, K. L. Gee, T. B. Neilsen, B. M. Harker, S. A. McInerny, R. L. McKinley, and M. M. James, "Investigation of multi-lobed fighter jet noise sources using acoustical holography and partial field decomposition methods," AIAA Paper 2015-2379 (2015).
[25]A. T. Wall, K. L. Gee, T. B. Neilsen, R. L. McKinley, and M. M. James, "Military jet noise source imaging using multisource statistically optimized near-field acoustical holography," J. Acoust. Soc. Am. **139**(4), 1938–1950 (2016).
[26]A. T. Wall, K. L. Gee, M. M. James, K. A. Bradley, S. A. McInerny, and T. B. Neilsen, "Near-field noise measurements of a high-performance military jet aircraft," Noise Control Eng. J. **60**, 421–434 (2012).
[27]M. Lee and J. S. Bolton, "Scan-based near-field acoustical holography and partial field decomposition in the presence of noise and source level variation," J. Acoust. Soc. Am. **119**, 382–393 (2006).
[28]J. S. Bendat, "Modern analysis procedures for multiple input/output problems," J. Acoust. Soc. Am. **68**, 498–503 (1980).
[29]A. T. Wall, K. L. Gee, and T. B. Neilsen, "Multisource statistically optimized near-field acoustical holography," J. Acoust. Soc. Am. **137**(2), 963–975 (2015).
[30]A. T. Wall, K. L. Gee, M. D. Gardner, T. B. Neilsen, and M. M. James, "Near-field acoustical holography applied to high-performance jet aircraft noise," Proc. Mtgs. Acoust. **9**, 040009 (2010).
[31]D. L. Hallman and J. S. Bolton, "A comparision of multi-reference near-field acoustical holography procedures," in *Proceedings of Noise-Con 94*, Ft. Lauderdale, FL (1994), pp. 929–933.
[32]H. S. Kwon and J. S. Bolton, "Partial field decomposition in nearfield acoustical holography by the use of singular value decomposition and partial coherence procedures," in *Proceedings of Noise-Con 98* (1998), pp. 649–654.
[33]T. A. Stout, K. L. Gee, T. B. Neilsen, A. T. Wall, and M. M. James, "Source characterization of full-scale jet noise using acoustic intensity," Noise Control Eng. J. **63**(6), 522–536 (2015).
[34]B. M. Harker, K. L. Gee, T. B. Neilsen, A. T. Wall, and M. M. James, "Beamforming-based wavepacket model for noise environment predictions of tactical aircraft," AIAA Paper 2017-4048 (2017).
[35]S. H. Swift, K. L. Gee, T. B. Neilsen, A. T. Wall, J. M. Downing, and M. M. James, "Spatiotemporal-correlation analysis of jet noise from a round nozzle high-performance aircraft," in *2018 AIAA/CEAS Aeroacoustics Conference* (accepted 2017).
[36]D. Papamoschou, "Wavepacket modeling of jet noise sources," AIAA Paper 2011-2835 (2011).
[37]R. H. Schlinker, R. A. Reba, J. C. Simonich, T. Colonius, K. Gudmundsson, and F. Ladeinde, "Towards prediction and control of large-scale turbulent structure supersonic jet noise," in *Proceedings of ASME Turbo Expo 2009* (2009).
[38]R. Reba, S. Narayanan, and T. Colonius, "Wave-packet models for large-scale mixing noise," Int. J. Aeroacoustics **9**, 533–558 (2010).
[39]T. B. Neilsen, K. L. Gee, A. T. Wall, and M. M. James, "Similarity spectra analysis of high-performance jet aircraft noise," J. Acoust. Soc. Am. **133**(4), 2116–2125 (2013).
[40]C. K. W. Tam, M. Golebiowsky, and J. M. Seiner, "On the two components of turbulent mixing noise from supersonic jets," AIAA Paper 96-1716 (1996).
[41]C. K. W. Tam and D. E. Burton, "Sound generated by instability waves of supersonic flows. Part 1. Two-dimensional mixing layers," J. Fluid Mech. **138**, 249–271 (1984).
[42]C. K. W. Tam and D. E. Burton, "Sound generated by instability waves of supersonic flows. Part 2. Axisymmetric jets," J. Fluid Mech. **138**, 273–295(1984).
[43]C. K. W. Tam, K. Viswanathan, K. K. Ahuja, and J. Panda, "The sources of jet noise: Experimental evidence," J. Fluid Mech. **615**, 253–292 (2008).
[44]K. Viswanathan, "Aeroacoustics of hot jets," J. Fluid Mech. **516**, 39–82 (2004).
[45]R. Reba, J. Simonich, and R. Schlinker, "Sound radiated by large-scale wave-packets in subsonic and supersonic jets," AIAA Paper 2009-3256 (2009).
[46]M. Kœnig, A. V. G. Cavalieri, P. Jordan, J. Delville, Y. Gervais, and D. Papamoschou, "Farfield filtering and source imaging of subsonic jet noise," J. Sound Vib. **332**(18), 4067–4088 (2013).
[47]P. J. Morris, "A note on noise generation by large scale turbulent structures in subsonic and supersonic jets," Int. J. Aeroacoustics **8**(4), 301–315 (2009).
[48]D. Papamoschou, "Prediction of jet noise shielding," AIAA Paper 2010-0653 (2010).
[49]T. B. Neilsen, A. B. Vaughn, K. L. Gee, M. Akamine, K. Okamoto, S. Teramoto, and S. Tsutsumi, "Level-educed wavepacket representation of Mach 1.8 laboratory-scale jet noise," AIAA Paper 2017-4049 (2017).
[50]T. B. Neilsen, K. L. Gee, B. M. Harker, and M. M. James, "Level-educed wavepacket representation of noise radiation from a high-performance military aircraft," AIAA Paper 2016-1880 (2016).